


 Cite this: *Chem. Commun.*, 2021, 57, 3255

 Received 28th December 2020,
 Accepted 15th February 2021

DOI: 10.1039/d0cc08377a

rsc.li/chemcomm

Oxygen doping in antimony sulfide nanosheets to facilitate catalytic conversion of polysulfides for lithium–sulfur batteries†

 Yonggui Zhang,^a Shuo Yang,^a *^{ab} Suya Zhou,^a Libin Zhang,^c Binbin Gu,^a Yangyang Dong,^a Suzhen Kong,^a Dong Cai,^a Guoyong Fang,^a ^a Huagui Nie^a and Zhi Yang ^a

A high-performance catalyst, O-doped Sb₂S₃ nanosheets (SS–O NSs), is synthesized and introduced into lithium–sulfur batteries. Owing to their good conductivity, strong adsorbability/catalytic effect to polysulfides and fast Li⁺ diffusion, the SS–O NSs-modified cathodes can effectively mitigate the shuttle effect, thus achieving outstanding electrochemical performance.

Lithium–sulfur (Li–S) batteries are regarded as the most promising power sources beyond lithium-ion batteries, due to their ultrahigh theoretical capacity (1675 mA h g^{−1}), low cost and environmental friendliness.¹ Nevertheless, the commercialization of Li–S batteries suffers from low utilization of sulfur, rapid capacity decay and poor cycling stability, which mainly stem from the notorious “shuttle effect” between the two electrodes brought about by the dissolution of intermediate lithium polysulfides (LiPSs) into the electrolyte.²

To overcome the aforementioned issues, great efforts have been devoted to sulfur cathode modification. In contrast with apolar carbon materials,³ applying polar materials, such as metal compounds,⁴ metals,⁵ and metal organic frameworks *etc.*,⁶ to the cathode design is more effective in weakening the shuttle effect of LiPSs by a strong chemical interaction. Among these materials, metal sulfides (*e.g.*, MoS₂, VS₂, CoS₂, Ni₃S₂) have shown promising applications in the Li–S battery field owing to their stronger sulfiphilic ability toward LiPSs and low lithiation voltages *vs.* Li/Li⁺.⁷ Nonetheless, the areal sulfur loading, long-term cycle stability and rate capability of the batteries with metal sulfide-based cathodes are still unsatisfactory due to their limited conductivity and longer Li⁺ diffusion path on

bulk metal sulfides.⁸ Therefore, atomic-scale development of new metal sulfide materials and fundamental understanding of the sulfur conversion mechanism on metal sulfide surfaces are urgently required for achieving high energy density and long cycle life in Li–S batteries.

Antimony sulfide (Sb₂S₃) exists widely in nature. The variable valence characteristic of a Sb cation can provide the possibility for a high catalytic effect.⁹ Recently, Sb₂S₃ has been widely utilized as a potential anode in sodium/lithium-ion batteries due to its excellent Li⁺/Na⁺ storage performance.¹⁰ It should also be a promising material applied in other electrochemical fields. Moreover, engineering nonmetallic atomic defects (doping/vacancies) into nanomaterials has been reported as an effective way to regulate its electronic structure, relieve polarization and increase the active sites to LiPSs, which in turn improves the device performance. It is found that an oxygen (O) atom has a suitable electron-regulating ability, which is not too strong to hamper Li⁺ diffusion and not too weak to trap the LiPSs *via* forming Li–O bonds.¹¹ Motivated by these studies, it is supposed that a high-performance catalyst for Li–S batteries can be achieved by constructing a hybrid architecture, O-doped Sb₂S₃. To our best knowledge, there are scarcely reported O-doped Sb₂S₃ cathode materials that can be applied in Li–S batteries.

In this work, the density functional theory (DFT) predictions of the structures of an O-doped Sb₂S₃ system and its ability to bind with LiPSs (Li₂S_{*n*}, *n* = 8, 6, 4, 2, 1) were firstly performed to verify the role of O-doped Sb₂S₃ in Li–S batteries. Clearly, O-doped Sb₂S₃ is most inclined to form the substituted O_{S1} on the surface (Fig. S2d, ESI†). Interestingly, after the S₁ atom is replaced by an O atom, the 3d electronic state of the Sb₂ atom shifts to lower energy, thus enabling a 0.12 eV reduced band gap of O-doped Sb₂S₃ than that of the pristine Sb₂S₃ (010) surface, as shown in Fig. 1a, which implies a higher electrical conductivity in O-doped Sb₂S₃. As presented in Fig. 1b and Fig. S3 (ESI†), after doping the surface with O atoms, more stable binding structures with the adsorption energies of −1.37–−2.96 eV are

^a Key Laboratory of Carbon Materials of Zhejiang Province, Wenzhou University, Wenzhou 325035, P. R. China. E-mail: yangshuo@wzu.edu.cn, yang201079@126.com

^b College of Electrical and Electronic Engineering, Wenzhou University, Wenzhou 325035, P. R. China

^c Hangzhou Electric Connector Factory, Hangzhou 310052, P. R. China

† Electronic supplementary information (ESI) available. See DOI: 10.1039/d0cc08377a

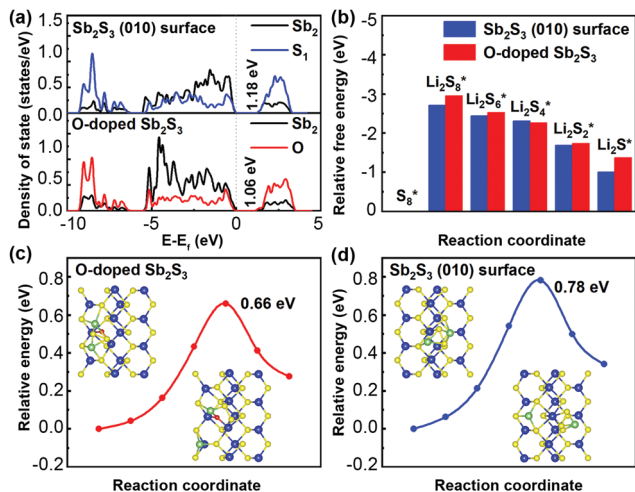


Fig. 1 (a) Electron densities of the state of undoped/O-doped Sb_2S_3 (010). All energies are referenced to the Fermi level (E_f). (b) The binding energies between Li_2S_n ($n = 8, 6, 4, 2, 1$) and undoped/O-doped Sb_2S_3 (010). Top views of Li migration routes and their relevant energy profiles of Li_2S_2 decomposition on (c) O-doped Sb_2S_3 and (d) a perfect Sb_2S_3 (010) surface. The blue, yellow, red, and green balls were Sb, S, O, and Li atoms, respectively.

obtained, where the S and Li atoms of LiPSs tend to chemically bond with the Sb and O atoms on O-doped Sb_2S_3 surfaces, respectively. These findings indicate that O-doped Sb_2S_3 could more effectively immobilize and convert LiPSs by creating more active sites, *i.e.*, S–Sb (S–metal) and Li–O (Li–nonmetal) coordinations, in agreement with the previous reports.^{7,10}

The Li^+ migration pathways and the corresponding energy profiles of the Li_2S_2 decomposition on pristine Sb_2S_3 (010) and O-doped Sb_2S_3 (010) surfaces were investigated by a climbing-image nudged elastic band (CI-NEB) method. As shown in Fig. 1c and d, the energy barriers for Li^+ diffusion along with bond breaking/forming on O-doped Sb_2S_3 surfaces (0.66 eV) are lower than the energy barriers on pristine Sb_2S_3 (0.78 eV) with the aid of the S–Sb and Li–O bonds. The results confirm that the deintercalation of Li^+ from Li_2S_2 to its adjacent location (*i.e.*, Li^+ transportation) on O-doped Sb_2S_3 surfaces becomes easier due to the presence of O, which contributes to the easier formation of abundant Li_2S on the concave surface of O-doped Sb_2S_3 .

Inspired by the exciting computational predictions, we developed a method of exfoliating pristine Sb_2S_3 in *N,N*-dimethylformamide (DMF) to obtain O-doped Sb_2S_3 nanosheets (SS–O NSSs), as shown in Fig. 2a (details are in the ESI†). Fig. 2b gives the UV–visible absorption spectra of the pristine Sb_2S_3 dispersed in 1-methyl-2-pyrrolidone (NMP) before and after exfoliation. Two distinct peaks at 276.5 and 344.6 nm are found in the spectrum after exfoliation. The former one is assigned to the excitonic absorption of the exfoliated Sb_2S_3 , which exhibits a blue-shift compared to the peak of pristine Sb_2S_3 (at 283.9 nm) due to the quantum confinement effect. The latter peak, which is not obvious in that of pristine Sb_2S_3 , might come from more defects generated during sonication.¹²

Furthermore, transmission electron microscopy (TEM) measurements were carried out. The low-resolution TEM images of

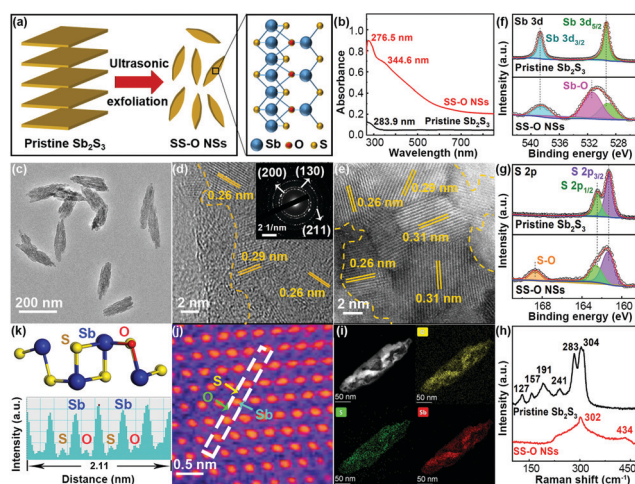


Fig. 2 (a) Synthetic scheme for SS–O NSSs. (b) UV–visible absorption spectra of pristine Sb_2S_3 and SS–O NSSs. (c) TEM, (d) HRTEM and (e) HAADF–STEM images of SS–O NSSs. Inset: SAED pattern of SS–O NSSs. The high-resolution (f) Sb 3d and (g) S 2p XPS spectra of pristine Sb_2S_3 and SS–O NSSs. (h) Raman spectra of pristine Sb_2S_3 and SS–O NSSs. (i) HAADF–STEM image and elemental mapping images of O, Sb and S for SS–O NSSs. (j) Selected area HAADF–STEM image of SS–O NSSs, and (k) the corresponding cross-sectional intensity of the atom contrast along with the structural model of SS–O NSSs.

the exfoliated Sb_2S_3 (Fig. 2c and Fig. S4, ESI†) demonstrate well-defined shuttle-shape nanosheets with a lateral size average of 200 nm and normal distribution, quite different from the morphology of pristine Sb_2S_3 (Fig. S5, ESI†). In the high-resolution TEM (HRTEM) (Fig. 2d) and the high-angle annular dark-field scanning transmission electron microscopy (HAADF–STEM) images (Fig. 2e), it is exciting to find that the exfoliated Sb_2S_3 surface is composed of randomly oriented amorphous textures at the edge and polycrystalline Sb_2S_3 features in the center. The distinct lattice fringes in Fig. 2d and e are slightly broader than those of pristine Sb_2S_3 (Fig. S6, ESI†),¹³ which might be caused by the changes of the perfect lattices to accommodate the curvature for the doping introduction into the crystallization domain. The selected area electron diffraction (SAED) pattern of the exfoliated Sb_2S_3 (inset of Fig. 2d) also validates that the nanosheets lose their single-crystal nature. The typical thickness of the Sb_2S_3 nanosheets was measured to be 1.5–3.0 nm by atomic force microscope (AFM) (Fig. S7, ESI†), equivalent to 1–2 Sb_2S_3 monolayers.¹⁴

Fig. 2f and g show the Sb 3d and S 2p X-ray photoelectron spectroscopy (XPS) analysis of the Sb_2S_3 . For pristine Sb_2S_3 , all the binding energies coincide with the reported values of Sb_2S_3 .¹⁵ While the exfoliated Sb_2S_3 appears markedly different. New peaks at 531.7 eV and 168.9 eV are observed, indicating the formation of Sb–O and S–O bonds.¹⁶ The results prove that O is implanted into the Sb_2S_3 nanosheets during exfoliation. The observed defect peak at 344.6 nm in the UV–visible absorption spectrum of the exfoliated Sb_2S_3 (Fig. 2b) thereby could be attributed to the introduction of O.

In Fig. 2h, the Raman spectrum of the exfoliated Sb_2S_3 reflects a dominant peak at 302 cm^{-1} whereas the absence of

other peaks for the well crystalline Sb_2S_3 .¹⁷ Compared to pristine Sb_2S_3 , the weaker and the broader peaks for the exfoliated Sb_2S_3 might be ascribed to the weaker interaction between the layers in the thinner layered- Sb_2S_3 . A new peak at 434 cm^{-1} emerged and is assigned to a Sb–O bond further confirming the existence of O in the Sb_2S_3 nanosheets.¹⁸

From energy dispersive X-ray spectroscopy (EDX) mapping results (Fig. 2i and Fig. S8a, ESI†), the O element is homogeneously dispersed in the product, further verifying the successful formation of SS–O NSs, while no O signal can be found in pristine Sb_2S_3 (Fig. S8b–e, ESI†). In the HAADF-STEM image (Fig. 2j), the darker spots (marked by yellow and green arrows) are distributed in the brighter atomic columns. The brighter spots (marked by blue arrows) can be assigned as Sb sites because of the higher atomic number of Sb than those of S and O. The corresponding cross-sectional intensity of the atom contrast in Fig. 2k shows the Sb/S/O intensity ratio of about 6:2:1, in accordance with the atomic numbers of Sb ($Z = 51$), S ($Z = 16$) and O ($Z = 8$). Obviously, O atoms locate at the lattice sites, implying the successful substitution of S atoms with O atoms in Sb_2S_3 nanosheets, in agreement with the calculations (Fig. S2d, ESI†).

Subsequently, the electrochemical performance of the SS–O NSs/carbon nanotubes (CNTs)-sulfur (S) cathode was evaluated in Li–S batteries. As found in the cyclic voltammograms (CVs) (Fig. 3a and Fig. S9, ESI†), the redox peaks of the SS–O NSs/CNTs-S cathode remain almost constant after activation (Fig. 3a), suggesting an excellent electrochemical reversibility. Compared with the pristine $\text{Sb}_2\text{S}_3/\text{CNTs-S}$ and CNTs-S cathodes, the SS–O NSs/CNTs-S cathode exhibits a stronger current density along with a positive/negative shift in the onset potentials of the reduction/oxidation peaks (Fig. 3b) and prominent rate capability (Fig. 3c), indicating that SS–O NSs can reduce the electrode polarization, inhibit the shuttle effect and accelerate the LiPS redox kinetics in Li–S batteries.¹⁹ In Fig. 3d, the galvanostatic charge/discharge profiles of the SS–O NSs/CNTs-S cathode at 0.2 C show two longer and flatter discharge platforms, which is consistent with the multistep reduction reaction of sulfur. The potential difference (ΔE_1) between the charge and discharge platforms in SS–O NSs/CNTs-S is much smaller than those in the other two cathodes (ΔE_2 and ΔE_3), reconfirming a lower polarization of the SS–O NSs/CNTs-S cathode.²⁰ The fast reaction kinetics, including faster interfacial electron transfer and Li^+ diffusion, for the SS–O NSs/CNTs-S cathode can be further confirmed by electrochemical impedance spectroscopy (EIS) experiments (Fig. S10 and Table S1, ESI†). In addition, the SS–O NSs/CNTs-S cathode is demonstrated to retain a good cycling stability upon long-term cycling. As illustrated in Fig. 3e, after 300 cycles at 2 C, the specific capacity of the SS–O NSs/CNTs-S cathode is still maintained at above 500 mA h g^{-1} , corresponding to a capacity fading rate of as low as 0.11% per cycle. Even with the high sulfur loading of 4.0 mg cm^{-2} , it can still hold a capacity of 657 mA h g^{-1} at the 120th cycle (Fig. S11, ESI†).

To fully understand the origin of the electrochemical improvements of the Li–S battery using the SS–O NSs/CNTs-S cathode, various (semi)-*in situ* spectroscopies were employed to

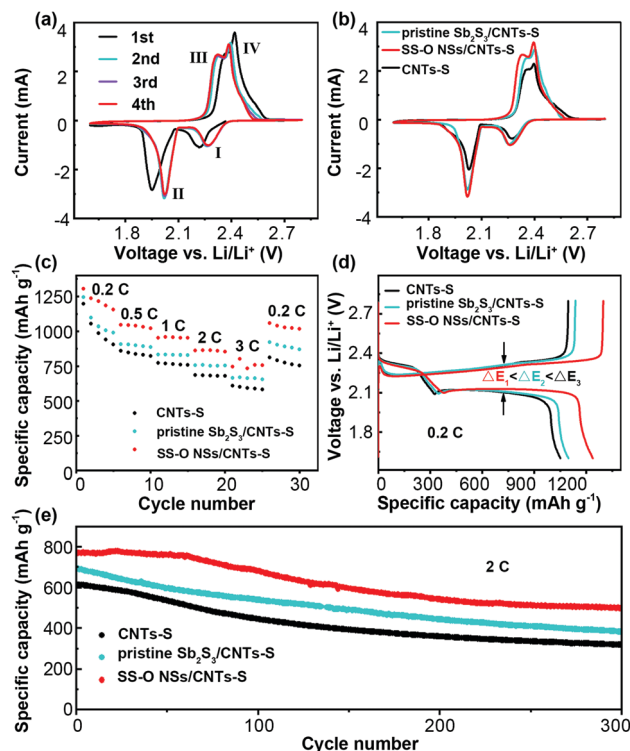


Fig. 3 (a) The initial four CVs of the SS–O NSs/CNTs-S cathode at 0.1 mV s^{-1} . (b) The second CVs of SS–O NSs/CNTs-S, pristine $\text{Sb}_2\text{S}_3/\text{CNTs-S}$ and CNTs-S cathodes at 0.1 mV s^{-1} . (c) Rate capabilities. (d) galvanostatic charge/discharge profiles for the second cycles at 0.2 C, and (e) cycling performance at 2 C (sulfur loading = 0.8 mg cm^{-2}) of SS–O NSs/CNTs-S, pristine $\text{Sb}_2\text{S}_3/\text{CNTs-S}$ and CNTs-S cathodes.

record the LiPS conversion during discharge and charge. In Fig. 4a, the semi-*in situ* XPS spectrum of the SS–O NSs/CNTs-S cathode shows the stronger signals of $\text{Li}_2\text{S}/\text{Li}_2\text{S}_2$, along with smaller proportions of Li_2S_n ($4 \leq n \leq 8$) at the end of discharge (1.6 V), in comparison to the pristine $\text{Sb}_2\text{S}_3/\text{CNTs-S}$ cathode (Fig. 4b), indicating that the SS–O NSs are very efficient in adsorption and fast conversion of long-chain polysulfides to short-chain polysulfides and improving the sulfur utilization. *In situ* UV–visible absorption spectra (Fig. S12, ESI†) during discharge also reveal that the SS–O NSs/CNTs-S cathode can accelerate the conversion of LiPSs. Furthermore, the prominent Li 1s peaks on the SS–O NSs/CNTs-S cathodes at different discharge states are shifted to a higher energy field (Fig. 4c) in contrast to the pristine $\text{Sb}_2\text{S}_3/\text{CNTs-S}$ cathode (Fig. 4d), indicating that the introduction of O into the Sb_2S_3 nanosheets could change the electronic interaction between Li^+ (or LiPSs) and SS–O NSs and promote the Li^+ transport for fast liquid–solid sulfur conversion kinetics.

In situ Raman results are shown in Fig. 4e, f and Fig. S13 (ESI†). The Li–O signal at 495 cm^{-1} is observed on the SS–O NSs/CNTs-S cathode during cycling (Fig. 4e and f). As the discharging proceeds, the S_3^{*} peak gradually disappears at 2.1 V (Fig. 4e) and reforms upon charging to 2.1 V (Fig. 4f). Interestingly, a new peak at 254 cm^{-1} due to S_3^{2-} starts to emerge at 2.3 V and grows during discharge (Fig. 4e),²¹ and then the intensity of the S_3^{2-} peak decreases and disappears

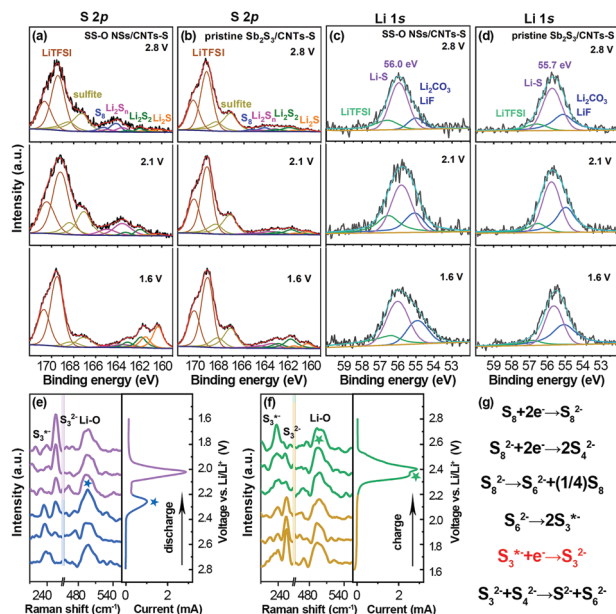


Fig. 4 Semi-*in situ* S 2p and Li 1s XPS spectra of (a and c) SS-O NSs/CNTs-S and (b and d) the pristine Sb₂S₃/CNTs-S cathode after discharge to specific states. *In situ* Raman spectra of (e) discharge and (f) charge processes of the SS-O NSs/CNTs-S cathode. (g) The proposed sulfur reduction reaction pathways on the SS-O NSs/CNTs-S cathode.

completely at 2.3 V with further charge (Fig. 4f). This manifests that the S₃^{*-} is reversibly turned to S₃²⁻ and reformed during cycling on the SS-O NSs/CNTs-S cathode. Such a result is also suggested by *in situ* UV-visible results (Fig. S12, ESI[†]), where the normalized absorbance for S₃^{*-} decreases with discharging, implying a consumption of S₃^{*-}. In contrast, for the pristine Sb₂S₃/CNTs-S cathode (Fig. S13c, ESI[†]), Raman signals for S₃²⁻ and Li-O are not observed, confirming the importance of SS-O NSs in suppressing shuttle effects and realizing a smooth solid-liquid-solid sulfur conversion reaction. With the observed improvement in electrochemical performance brought by O doping, it can be inferred that the introduction of O atoms into the system is likely to change the sulfur reduction reaction pathways on the cathode surface, where the observed new S₃²⁻ species, as an important intermediate for promoting liquid-solid sulfur conversion, might be the result of the reactions²² as shown in Fig. 4g. Such a new reaction pathway on the SS-O NS surface probably needs less energy than on pristine Sb₂S₃, which is favorable for proceeding fast liquid-solid sulfur conversion reaction.

In conclusion, we successfully developed an efficient SS-O NS catalyst through a tip-sonication of pristine Sb₂S₃ in DMF. The O doping and nanostructural engineering in Sb₂S₃ improves its electrical conductivity, sulfiphilic/catalytic characters with LiPSs through S-Sb and Li-O bonds, and accelerates the Li⁺ diffusion. As a result, the SS-O NSs/CNTs-S cathode demonstrates high efficiency in suppressing polysulfide shuttling and promoting sulfur redox kinetics in terms of specific capacity, rate capability and long-term cycling performance.

The (semi)-*in situ* spectroscopic studies and DFT calculations further confirm the structure-reactivity correlation at the cathode surface, and a new sulfur reduction reaction mechanism is also proposed. This study will offer guidance on doping engineering for the simultaneous realization of good electrical/ionic conductivity, high adsorbability/catalytic activity and fast Li⁺ diffusion in Li-S cathodes.

This work was supported in part by grants from the National Natural Science Foundation of China (51972238 and 21875166), Zhejiang Provincial Natural Science Foundation of China (LR18E020001 and LQ19B030006), Science and Technology Project of Zhejiang Province (LGF18B050005), and Basic Scientific Research Projects of Wenzhou City (G2020002).

Conflicts of interest

There are no conflicts of interest to declare.

References

- X. Zhang, K. Chen, Z. Sun, G. Hu, R. Xiao, H.-M. Cheng and F. Li, *Energy Environ. Sci.*, 2020, **13**, 1076–1095.
- H. Yuan, J.-Q. Huang, H.-J. Peng, M.-M. Titirici, R. Xiang, R. Chen, Q. Liu and Q. Zhang, *Adv. Energy Mater.*, 2018, **8**, 1802107.
- C. Ye, D. Chao, J. Shan, H. Li, K. Davey and S.-Z. Qiao, *Matter*, 2020, **2**, 323–344.
- Z. Shen, M. Cao, Z. Zhang, J. Pu, C. Zhong, J. Li, H. Ma, F. Li, J. Zhu, F. Pan and H. Zhang, *Adv. Funct. Mater.*, 2019, **30**, 1906661.
- Y. Li, C. Wang, W. Wang, A. Y. S. Eng, M. Wan, L. Fu, E. Mao, G. Li, J. Tang, Z. W. Seh and Y. Sun, *ACS Nano*, 2020, **14**, 1148–1157.
- W. Li, J. Qian, T. Zhao, Y. Ye, Y. Xing, Y. Huang, L. Wei, N. Zhang, N. Chen, L. Li, F. Wu and R. Chen, *Adv. Sci.*, 2019, **6**, 1802362.
- D. Guo, Z. Zhang, B. Xi, Z. Yu, Z. Zhou and X. Chen, *J. Mater. Chem. A*, 2020, **8**, 3834–3844.
- C. Zhang, S. Liu, G. Li, C. Zhang, X. Liu and J. Luo, *Adv. Mater.*, 2018, **30**, 1801328.
- Y. Zhang, J. Deng, H. Zhang, Y. Liu and H. Dai, *Catal. Today*, 2015, **245**, 28–36.
- S. Yao, J. Cui, J. Q. Huang, Z. Lu, Y. Deng, W. G. Chong, J. Wu, M. Ihsan Ul Haq, F. Ciucci and J. K. Kim, *Adv. Energy Mater.*, 2018, **8**, 1800710.
- K. Park, J. H. Cho, J.-H. Jang, B.-C. Yu, A. T. De La Hoz, K. M. Miller, C. J. Ellison and J. B. Goodenough, *Energy Environ. Sci.*, 2015, **8**, 2389–2395.
- L. Cao, S. Emami and K. Lafdi, *Mater. Express*, 2014, **4**, 165–171.
- E. Dutková, L. Takacs, M. J. Sayagués, P. Baláž, J. Kováč and A. Šatka, *Chem. Eng. Sci.*, 2013, **85**, 25–29.
- S. Yao, J. Cui, Y. Deng, W. G. Chong, J. Wu, M. Ihsan-Ul-Haq, Y.-W. Mai and J.-K. Kim, *Energy Storage Mater.*, 2019, **20**, 36–45.
- H. Wang, X. Yuan, H. Wang, X. Chen, Z. Wu, L. Jiang, W. Xiong and G. Zeng, *Appl. Catal., B*, 2016, **193**, 36–46.
- H. Lei, T. Lin, X. Wang, S. Zhang, Q. Cheng, X. Chen, Z. Tan and J. Chen, *Mater. Lett.*, 2018, **233**, 90–93.
- J. S. Eensalu, A. Katerski, E. Kärber, I. Oja Acik, A. Mere and M. Krunks, *Beilstein J. Nanotechnol.*, 2019, **10**, 198–210.
- E. Kärber, A. Katerski, I. Oja Acik, A. Mere, V. Mikli and M. Krunks, *Beilstein J. Nanotechnol.*, 2016, **7**, 1662–1673.
- X. Ding, S. Yang, S. Zhou, Y. Zhan, Y. Lai, X. Zhou, X. Xu, H. Nie, S. Huang and Z. Yang, *Adv. Funct. Mater.*, 2020, **30**, 2003354.
- S. Zhou, S. Yang, X. Ding, Y. Lai, H. Nie, Y. Zhang, D. Chan, H. Duan, S. Huang and Z. Yang, *ACS Nano*, 2020, **14**, 7538–7551.
- M. Hagen, P. Schiffels, M. Hammer, S. Dörfler, J. Tübke, M. J. Hoffmann, H. Althues and S. Kaskel, *J. Electrochem. Soc.*, 2013, **160**, A1205–A1214.
- Q. Zou and Y. C. Lu, *J. Phys. Chem. Lett.*, 2016, **7**, 1518–1525.